ROYAL SOCIETY
OF CHEMISTRY

PAPER

Check for updates

Densification and performance optimization of NaSICON solid electrolytes *via* a low-temperature cold sintering process with sodium ionic salt doping†

Sergio Ferrer-Nicomedes, [iD] [ab] Andrés Mormeneo-Segarra, [iD] [ab] Nuria Vicente-Agut [iD] *[ab] and Antonio Barba-Juan [iD] [ab]

Sodium-ion batteries (SIBs) have emerged as a sustainable alternative to lithium-ion systems, offering cost-effective and environmentally friendly energy storage solutions. Solid-state electrolytes (SSEs), particularly NaSICON-type materials such as $Na_{3.4}Zr_{1.9}Zn_{0.1}Si_{2.2}P_{0.8}O_{12}$ (NZZSP) studied here, are critical for enhancing the safety and stability of SIBs. However, conventional high-temperature sintering methods for fabricating these electrolytes are energy-intensive and environmentally impactful. In this work, we employed the Cold Sintering Process (CSP) to densify NZZSP at a low temperature of 150 °C under 720 MPa with the aid of a transient liquid phase (TLP), achieving a sustainable electrolyte production with competitive performance. The effects of milling time and two different TLP media were evaluated, with 3 M acetic acid solution (HAc) being more effective than 25 mM sodium hydroxide solution (NaOH) in preserving particle integrity and yielding higher ionic conductivity (0.50 mS cm^{-1}). Doping with $NaPF_6$ and NaTFSI further enhanced performance, with 20% $NaPF_6$-doped samples achieving the highest densification (94.3%) and conductivity (0.80 mS cm^{-1}). Optimized 2 hour-milled, 20% $NaPF_6$ electrolytes demonstrated suitable cycling stability in symmetric cells (over 500 hours) and specific capacity in half cells, with Na metal and $Na_3V_2(PO_4)_3$ (NVP) as electrodes, of about 85 mA h g$_{NVP}^{-1}$ at C/2 and over 100 mA h g$_{NVP}^{-1}$ at C/10 after cycling at multiple rates. These results underscore the potential of the CSP as a sustainable, low-temperature alternative for fabricating high-performance solid-state electrolytes for application in all solid-state sodium batteries.

Introduction

The increasing global demand for efficient and sustainable energy storage technologies has intensified research into advanced and more sustainable battery materials. Lithium-ion batteries (LIB), while being widely employed in modern devices, start to face challenges such as resource scarcity, safety concerns related to the use of liquid organic electrolytes, and the environmental impact associated with them.[1,2] To address the availability issues of lithium-based components, sodium-ion batteries (SIBs) emerged as a promising alternative, leveraging the abundance and low cost of sodium compared to lithium.[3,4] This abundance translated into reduced material costs and mitigated supply chain vulnerabilities associated with lithium. Furthermore, SIBs offered a more sustainable option

for large-scale energy storage due to their compatibility with environmentally friendly materials.[5]

In addition to reducing the cost of sodium-based energy storage, devices, a notable advantage of SIBs is their higher compatibility with solid-state electrolytes (SSEs), which allow the replacement of conventional liquid organic electrolytes.[6,7] Hence, solid-state electrolytes enhance battery safety by eliminating flammable components, thereby reducing the risk of thermal runaway. They also offered environmental benefits by avoiding toxic organic solvents, aligning with the need for greener energy storage solutions.[8] Several materials have been studied as promising solid electrolytes, from the traditional β-alumina-type electrolytes to modern hydride- and halide-based sodium electrolytes.[9,10] Among these materials, NaSICON (Sodium Super Ionic Conductor) electrolytes have been particularly noteworthy due to their high ionic conductivity, structural stability, and versatility.[11,12] Indeed, recent studies have demonstrated that compositional tailoring, such as doping, effectively improved the ionic conductivity and electrochemical stability of NaSICON-type materials, emphasizing their suitability for SIB applications, as for example in the case of the Hf-

aChemical Engineering Department, Universitat Jaume I, 12071, Castelló de la Plana, Spain. E-mail: vicenten@uji.es

bInstituto Universitario de Tecnología Cerámica, Universitat Jaume I, 12071, Castelló de la Plana, Spain

This journal is © The Royal Society of Chemistry 2025

J. Mater. Chem. A, 2025, **13**, 12439–12451 | 12439

modified NASICON electrolyte with the formula $Na_{3.2}Hf_{1.9}$-$Ca_{0.1}Si_2PO_{12}$ that achieved an ionic conductivity of 1 mS cm^{-1} when sintered at high temperature.[13–16]

However, conventional sintering methods for fabricating such solid electrolytes require elevated temperatures commonly over 1000 °C, which imply significant energy consumption and associated carbon emissions. To address these issues, the Cold Sintering Process (CSP) technique has emerged as an innovative alternative. The CSP has been proved to enable the densification of inorganic materials at significantly lower temperatures (below 300 °C) through the application of pressure (hundreds of MPa) and a transient liquid phase (TLP).[17] This technique achieves densification of the ceramics thanks to the TLP, which dissolves the grain boundaries of particles, favours the mass transfer from grain boundaries to the pores due to the gradient in concentration generated by high pressures and when evaporated because of the temperature applied, enables the precipitation and densification of the ceramic samples.[18] Previous studies demonstrated that the CSP is an effective tool for producing dense, highly conductive structures in NaSICON-type and other ceramic materials without compromising their electrochemical properties in the field of solid electrolytes.[19–22]

In this work, we employed the CSP to fabricate NaSICON solid electrolytes for their potential application in greener all solid-state sodium batteries (ASSNBs). The composition of the ceramics employed was based on the well-known $Na_{1+x}Zr_2Si_x$-$P_{3-x}O_{12}$ ($0 \leq x \leq 3$) structure, with slight modifications to substitute Zr^{4+} by aliovalent Zn^{2+} and P^{5+} by Si^{4+}, in order to obtain a more stable and highly conductive SSE, with the molecular formula $Na_{3.4}Zr_{1.9}Zn_{0.1}Si_{2.2}P_{0.8}O_{12}$ (NZZSP).[23,24] We investigated how milling time influenced the particle size and particle distribution of the ceramics, which governs the microstructure generated by cold sintering. Moreover, the effect of acidic and alkaline media on the CSP was studied by employing two different TLPs, namely acetic acid (HAc) and sodium hydroxide (NaOH), and how it affected the structural and electrochemical properties of the solid electrolytes produced. Additionally, the solid electrolytes were then doped

with ionic conductive salts through the CSP, specifically $NaPF_6$ and NaTFSI, to evaluate if their incorporation influenced the sodium ion conductivity once deposited on the grain boundaries of the ceramics, similar to the case in which sodium-based additives (*i.e.* NaF) are used to improve the grain boundary conductivity of the electrolytes.[25–27] Finally, the doped electrolytes that showed an improvement in the electrochemical properties were subjected to electrochemical cycling under operational conditions (symmetric and half-cells) to evaluate their suitability as solid-state sodium electrolytes. This comprehensive approach contributed to the development of safer, more sustainable, and efficient solid-state sodium-ion batteries.

Experimental

NaSICON powder synthesis

The NaSICON powder was synthesized by a solid-state reaction with a modified route adapted from Yang, J. *et al.*[23] Na_2CO_3 (Sigma-Aldrich, 99.5%), ZrO_2 (Alfa-Aesar, 99%), ZnO (Sigma-Aldrich, 99.9%), SiO_2 (Sigma-Aldrich, 99.8%) and $(NH_4H_2)PO_4$ (Sigma-Aldrich, 99.9%) were employed as the precursors in a weight ratio of 1.96 : 2.54 : 0.09 : 1.44 : 1 to obtain the stoichiometry of the NaSICON structure. The precursor powders were ball milled in absolute ethanol in a planetary ball mill for 4 h at 300 rpm. For the milling, agate jars and zirconia balls are used, with a ball weight to precursor powder ratio of 3.67 : 10 : 1, for balls 10 mm and 5 mm in diameter, respectively. After milling, the precursor suspension is dried under vacuum for 12 h at 80 °C to remove ethanol. The dried powder was loaded in alumina crucibles and the solid-state reaction was performed in a muffle furnace in an air atmosphere. The powder was brought to 1000 °C for 4 h with a 5 °C min^{-1} rate, and immediately after this the temperature was increased to 1200 °C for 10 h to synthesize the NaSICON powder. Fig. S1† shows the XRD pattern of the as-synthesized powder, which coincides with the NZSP standard pattern. Afterwards, the NaSICON powder was ball-milled for 10′ (0 h), 2 h, 4 h and 6 h, under the same milling conditions as
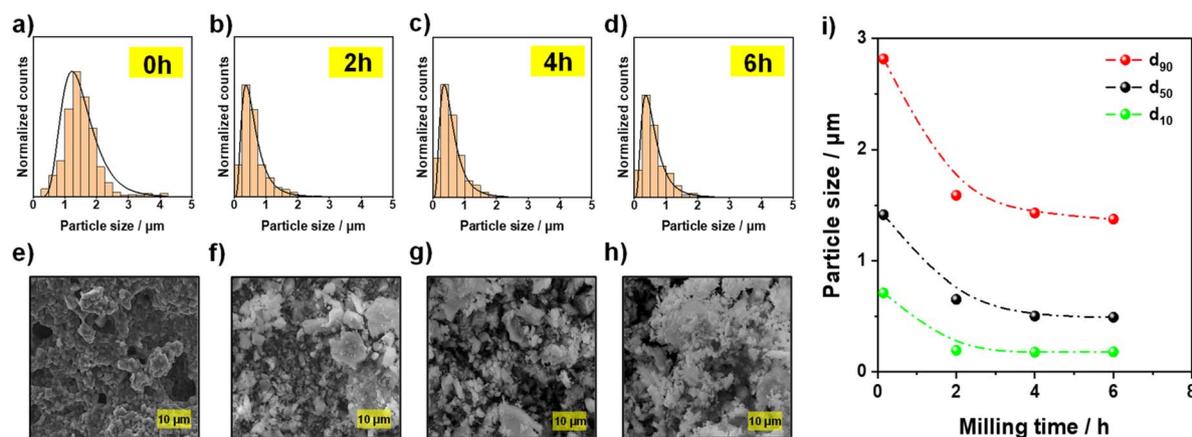

Fig. 1 (a–d) Particle size distribution of the NZZSP powder after milling for 10 minutes, and 2, 4 and 6 hours (0 h, 2 h, 4 h and 6 h, respectively). (e–h) SEM images of the 0 h, 2 h, 4 h and 6 h powders. (i) 10, 50 and 90 percentiles (d_{10}, d_{50} and d_{90}, respectively) of the particle size as a function of the milling time.

12440 | *J. Mater. Chem. A*, 2025, 13, 12439–12451

This journal is © The Royal Society of Chemistry 2025

those for the precursors, in order to obtain different particle sizes for the microstructural study. The 0 h milling-time series had a 10′ milling for simply breaking agglomerates. Fig. 1(a)–(d) show the particle size distribution of each milling time and the d_{10}, d_{50} and d_{90} (10, 50 and 90 percentiles of particle size) with a log-normal fitting. Also, Fig. 1(i) summarizes the effect of the milling time on the particle size of the powders. For the measurement of the particle size, at least 500 measurements were made in SEM pictures of each powder with the ImageJ (NIH) software.

Cold sintering process

For the densification of the powders, the cold sintering process was used. The CSP conditions selected for this work were based on the suitability of the mild conditions previously employed by the authors for the sintering of other NaSICON-like ceramics, such as $Li_{1.3}Al_{0.3}Ti_{1.7}(PO_4)_3$ (LATP).[28] Here, the sintering temperature was 150 °C, with a dwell time of 90 min for the sintering process and a maximum pressure of 720 MPa. For the TLP study, two complementary solutions in the pH scale were tested: a 3 M acetic acid (HAc) solution (pH ≈ 2) and a 25 mM NaOH solution (pH ≈ 12) to evaluate the effect of complementary acidic and basic media on the sintering and the final properties. To perform the CSP, the NaSICON powder was manually ground in an agate mortar in the presence of 15 wt% of TLP to wet the powder. Once the powder was homogenized, it was loaded into a custom-made hardened steel mould to conduct the CSP with an XRPress MT25 hand press from XRF Scientific. Two aluminium collectors and Kapton tape were employed to conduct the electrochemical impedance spectroscopy (EIS) on each electrolyte under *operando* conditions. Further experimental details about the set up can be checked in Fig. S2 and S3.† After the CSP, the obtained samples are fine polished employing SiC sandpaper of 600, 800, 1000, 1500 and 2500 grit until a smooth surface is obtained. All the series of CSEs in this work have three replicas and present a thickness of 1.30 ± 0.05 mm and a diameter of 7.8 mm. For the evaluation of the doping effect with sodium ionic salts, the CSP conditions and the preparation were kept the same. The only difference was that the ionic salts were incorporated into the composition through the TLP, to obtain wetted powders with 10 and 20 wt% of the total mass corresponding to the doping agents. To do so, 3 M HAc solutions with different salts were prepared by adding an appropriate amount of NaTFSI (99%, Sigma-Aldrich) and NaPF₆ (98%, Sigma-Aldrich) so that 15 wt% of TLP employed in the CSP preparation could easily incorporate the dopants.

Microstructural characterization

For the evaluation of the microstructure of the solid electrolytes, different techniques were used. Scanning Electron Microscopy (SEM) (FEG-SEM Quanta 200F) and Transmission Electron Microscopy (TEM) (Jem-2100 LaB6, JEOL) were mainly employed to characterize the particles and the changes occurring in the microstructure after the CSP. Also, an Olympus SZX16 optical microscope equipped with an Olympus SC50 digital camera was used to obtain images of the surface of cycled solid electrolytes. X-ray diffraction (XRD) (Advance diffractometer, Bruker Theta-Theta, Germany) with Ni-filtered Cu Kα radiation (Kα₁ = 1.540598 Å) between 5° and 90° was used to obtain the crystalline pattern of the structures, and DIFFRAC.EVA (Bruker) software and the ICSD and ICDD databases were used to analyse the patterns. To calculate the real density of the powders, a helium pycnometer was employed. For the case of the as-synthesized NZZSP powder, the density was 3.17 ± 0.04 g cm^{-3}, and for the doped NZZSP powders the density was calculated with the rule of mixtures considering the density of each component and its mass fraction. In order to obtain the relative density of the solid electrolytes, the Archimedes' immersion method was used in a mercury medium, and the relative density (φ) was calculated with eqn (1), where m_{SE}, m_{Hg}, ρ_{Hg} and ρ_{SE} are the mass of the dried solid electrolyte, the mass of the solid electrolyte immersed in mercury, the density of the solid electrolyte material and the density of mercury, respectively.

$$\varphi \ (\%) = \frac{m_{SE}\rho_{Hg}}{m_{Hg}\rho_{SE}} \times 100 \tag{1}$$

Electrochemical characterization

As part of the electrochemical characterization, the CSP setup is equipped with a Multi Autolab M204 potentiostat (Metrohm) with an impedance module to conduct the *operando* EIS in the frequency range of 1 MHz to 10 Hz. All the impedance data are analysed with ZView4 software from Scribner (with a tolerance of 5%). A generic Nyquist and Bode plot of the EIS spectra and the equivalent circuit employed are shown in Fig. S4,† to model the EIS response and characterise the effect of the TLPs and ionic salts on the total resistance of the samples, with R_b being the bulk NZZSP resistance and R_{gb}, the grain boundary resistance. This last one accounts for the bare grain boundaries and for the grain boundaries with the ionic salts deposited when they are employed to enhance ionic transport. During the natural cooling process of the CSP, for each solid electrolyte produced, EIS spectra are registered and analyzed until room temperature to obtain valuable information about the activation energy and the ionic conductivity.[29] The ionic conductivity (σ) can be calculated with eqn (2), where t and S represent the thickness and the surface area of the sample, respectively, and R is the total resistance obtained from the fitting of the Nyquist plot. In order to calculate the activation energy, the modified Arrhenius fitting shown in eqn (3) can be used, where A, k_B, E_a and T are the preexponential factor, the Boltzmann constant, the activation energy and the temperature, respectively.

$$\sigma = \frac{t}{RS} \tag{2}$$

$$\sigma T = A e^{-\frac{E_a}{k_B T}} \tag{3}$$

Symmetric cells (Na|NZZSP|Na) were assembled using sodium metal (PI-KEM, 99.9%, 0.45 mm thick) as the electrode and 5 μL of 1 M NaPF₆ in EC : PC (1 : 1 vol%) to improve the interfacial contact between the components of the cell. For the characterization of the electrochemical response of the

This journal is © The Royal Society of Chemistry 2025

J. Mater. Chem. A, 2025, **13**, 12439–12451 | **12441**

electrolytes under operating conditions, half-cells with $Na_3V_2(PO_4)_3$ (NVP, PI-KEM, 99.9%) as the cathode were employed. The cathode composition presented a mass ratio of 8:1:1 of NVP, polyvinylidene fluoride (PVDF) and carbon Super-P, previously dispersed in N-methyl-2-pyrrolidone (NMP) and deposited on a 25 µm aluminium foil. After vacuum drying the deposited electrodes for 12 h at 110 °C, the cathodes presented a mass loading of 4 mg cm^{-2}. All samples tested were assembled in 3/8″ Swagelok-type PFA cells inside a glovebox filled with Ar (O_2 and H_2O levels below 0.1 ppm) and the cycling rates were set considering the theoretical specific capacity of NVP (117.6 mA g$_{NVP}^{-1}$).

Results and discussion

Particle size and transient liquid phase dependence

Different particle sizes and distributions were produced with milling times of 0, 2, 4 and 6 hours, as shown in Fig. 1. Previous studies by the group demonstrated that both the particle size distribution and transient liquid phase significantly influenced the sintering and thus the final properties of a NaSICON-type material, LATP, when processed by cold sintering.[30,31] Hence, the effect of the NZZSP particle size distribution was evaluated in parallel with the presence of two types of TLP during the CSP. For this, 3 M acetic acid solution (HAc, pH = 2) was employed as it was reported to be an excellent transient liquid phase for the CSP, and 25 mM sodium hydroxide (NaOH, pH = 12) was tested since it was a sodium-based base solution which, due to its sodium nature, could provide optimum conditions for sintering. After the cold sintering of at least three solid electrolytes per series of milling time (particle size distribution) and TLP, the mean value of densification for each series is presented in Fig. 2, as a measure of the sintering degree. Overall, it was observed that both TLPs ensure the densification of the solid

electrolytes, reaching values of relative density above 80%. Also, no notable effect was observed from the particle size distribution, as the ratio of great (d_{90}) and fine (d_{10}) particles remained similar at every milling time. Nonetheless, it is worth noting that for every particle size distribution the relative density of the series produced with NaOH as the TLP presents a slightly higher value.

In order to obtain further information about the relationship between the microstructure generated and the electrochemical properties of the SSEs, the ionic conductivity and activation energy were calculated through electrochemical impedance spectroscopy during the cooling process of each sample processed by the CSP. Fig. 3(a) and (b) show the Nyquist plot at room temperature and the fitting of the data for one series of samples cold sintered with HAc and NaOH, respectively. It is immediately observed that samples prepared with acetic acid presented lower resistance values than those prepared with sodium hydroxide. Also, in Fig. 3(c) the mean ionic conductivity values of the three replicas at RT and the activation energies are plotted as a function of the milling time (and therefore the particle size distribution). The ionic conductivity of the NZZSP electrolytes exhibited the same behaviour as those prepared with LATP in previous studies of the group: a decay of the ionic conductivity as the particle size decreased, demonstrating the strong dependence of ionic conductivity on the microstructure generated with the CSP. This can be understood if the grain boundary effect is considered. In the CSP, larger particles tend to generate a microstructure with a lower amount of grain boundaries, arising from the mass transport aided by the TLP in the particle–particle contact area. Conversely, smaller particles tend to generate more compact microstructures (with the proper particle size distribution, as in the present case, Fig. 1) but with the generation of more surface area in between particles, that is the grain boundary. In this particular case, longer milling times generate particle sizes and distributions twice as small as the bigger ones. Since the grain boundaries on the particles are the limiting step for ionic transport, particularly in the CSP, the similarity in the trend between ionic conductivity and the particle size is understood. Furthermore, it was observed that in all of the SSEs prepared, the ionic conductivity of the HAc series was higher than that of the NaOH electrolytes, suggesting that although both TLPs lead to similar densification values, any variation in the microstructure produced as a result of the TLP was leading to differences in the conduction of the Na$^+$ ions. Regarding the activation energy values, they did not have the same tendency as the particle size distribution. Although the NaOH series might present some values higher than that of the same milling times series but prepared with HAc, all values were in the range of 0.27–0.31 eV with a pattern suggesting that the E_a could be constant for these SSEs prepared by the CSP (Arrhenius plots for the calculation are shown in Fig. S5†). Table 1 summarizes the electrochemical results with the microstructure parameters measured.

To deepen into the phenomenon behind the difference in ionic conductivity when NZZSP electrolytes were processed with an acid or a basic medium in the CSP, further characterization was performed. X-ray diffraction was performed for all series of
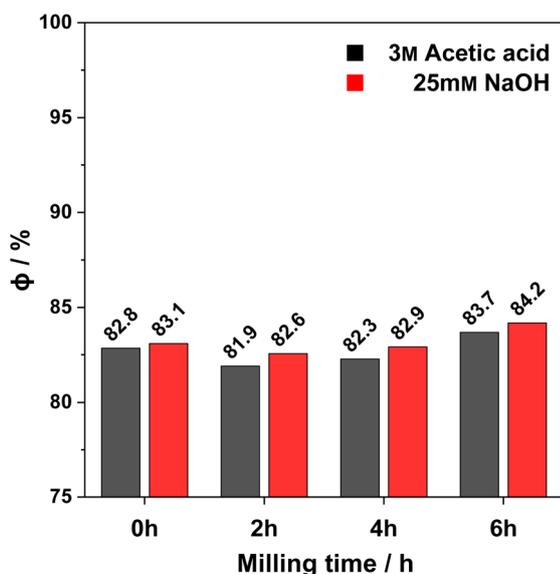

Fig. 2 Dependence of the relative density of the NZZSP solid-state electrolytes on the powder milling time and the TLP media.
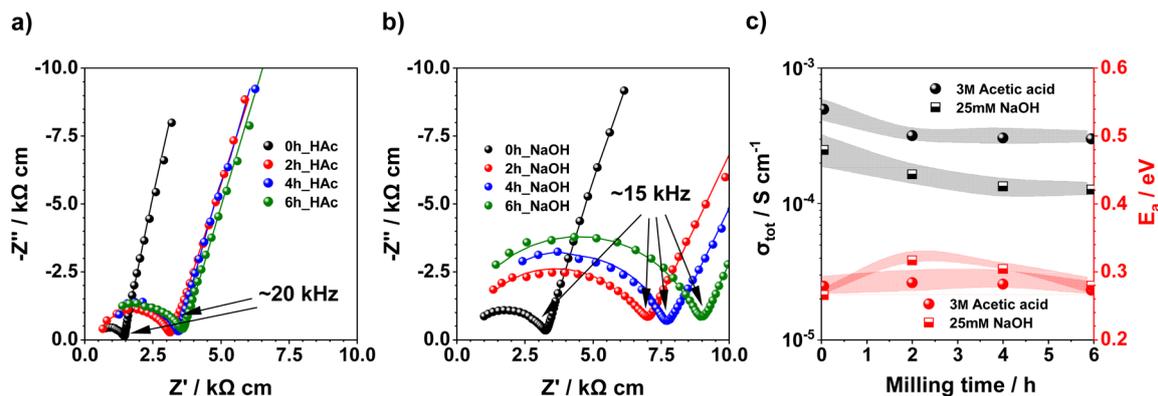
12442 | J. Mater. Chem. A, 2025, **13**, 12439–12451

This journal is © The Royal Society of Chemistry 2025

Fig. 3 (a and b) Nyquist spectra and fitting for each NZZSP milling time from the series of solid electrolytes cold sintered with acetic acid (HAc) and sodium hydroxide (NaOH). (c) Mean ionic conductivity and activation energy for the samples as a function of the NZZSP milling time. The shadow area represents the dispersion of the replicas. The equivalent circuit employed for the fitting is shown in Fig. S4.†

Table 1 Summary of the mean relative density, ionic conductivity, activation energy and particle size distribution as a function of the milling time and TLP employed in the CSP

	HAc_series				NaOH_series			
t_{mill} (h)	0	2	4	6	0	2	4	6
d_{10} (μm)	0.71	0.20	0.18	0.18	0.71	0.20	0.18	0.18
d_{50} (μm)	1.42	0.65	0.50	0.49	1.42	0.65	0.50	0.49
d_{90} (μm)	2.81	1.59	1.43	1.38	2.81	1.59	1.43	1.38
φ (%)	82.8	81.9	82.3	83.7	83.1	82.6	82.9	84.2
σ (mS cm^{-1})	0.50	0.32	0.31	0.30	0.25	0.17	0.14	0.13
E_a (eV)	0.28	0.28	0.28	0.27	0.27	0.31	0.30	0.28

electrolytes produced, and the results are shown in Fig. 4. In general, all XRD patterns were similar to the standard pattern of Na$_3$Zr$_2$Si$_2$PO$_{12}$ (ICSD #473), despite presenting small amounts of monoclinic ZrO$_2$, a common and highly reported secondary phase produced during the solid-state synthesis, which can even be beneficial for the stability of the crystal structure of the NZSP at RT.[32–34] Also, the intensity of the peaks tended to decrease and turned wider as the milling time increased, identical to the behaviour of the LATP particle case already reported by the group.[35] However, an unexpected peak became distinguishable at 30° in all the XRD patterns of the SSEs prepared with NaOH as the TLP. Although the new peak was observable, its intensity was not enough to precisely determine which phase it could belong to, but the imprints suggested that it could be sodium phosphate phases (NaPO$_3$, Na$_5$P$_3$O$_{10}$ and Na$_3$PO$_4\cdot$12H$_2$O). Since the liquid phase employed during the sintering was NaOH, it is suggested that the aggressive conditions of the basic media not only triggered the sintering mechanism of the CSP, but also caused the surface of the
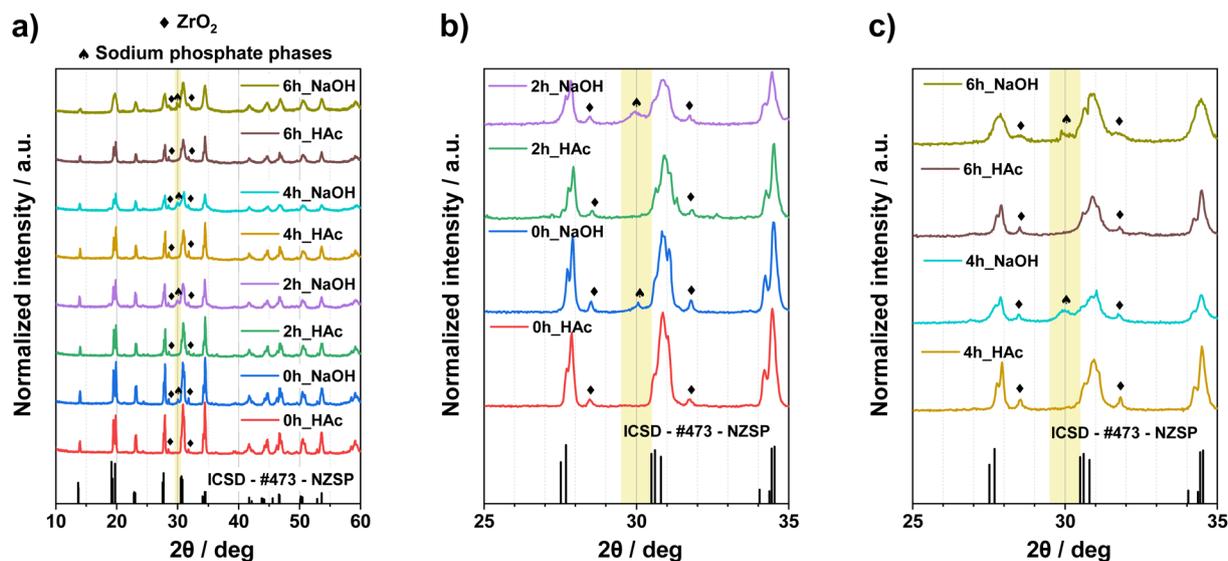

Fig. 4 (a) X-ray diffractograms of the NZZSP powders for both transient liquid phases and ICSD #473 XRD pattern of Na$_3$Zr$_2$Si$_2$PO$_{12}$. (b and c) Detailed view of the 30-degree XRD peak for the solid electrolytes showing a new peak for the NaOH series.

This journal is © The Royal Society of Chemistry 2025

J. Mater. Chem. A, 2025, **13**, 12439–12451 | **12443**

particles to be attacked leading to new phases which could influence the electrochemical behaviour of the SSEs.

In order to validate this hypothesis, the microstructure of the solid electrolytes and their particles were carefully analyzed by means of electron microscopy in SSEs cold sintered with both TLPs, in this case for the 2 h series. TEM images of the NZZSP particles after the CSP revealed a key difference between the series, as shown in Fig. 5(a) and (b). Both images showed the grain boundary of two sintered NZZSP particles, with a defined bottleneck that appears between them demonstrating the densification mechanism of the CSP in the frame of the pressure solution creep theory.[18] Although grain boundaries of the particles sintered with HAc showed a higher degree of crystallinity, those of the particles densified with the aid of NaOH suggested that structural modifications occurred during the solution-precipitation mechanism of the CSP. Although the grain boundary between particles processed with NaOH seemed to be homogeneous, the difference in crystallinity confirmed that microstructural changes occurred during the sintering and lead to the formation of secondary phases in the grain

boundaries. Ideally, the TLP employed in the CSP should be able to dissolve the grain boundaries of the particles, and when evaporated enable the material to precipitate without any crystalline phase modification leading to densification, as was previously demonstrated to occur with acetic acid. However, it has also been reported that under high pressures, strong basic media could lead some chemical species to compete for the formation of new phases, as proved in the case of $BaTiO_3$ in the presence of the $Sr(OH)_2 \cdot 8H_2O$ strong alkali.[36] Alternatively, higher concentrations of NaOH as the TLP during the cold sintering of similar NZSP ceramics have been tested (1 M NaOH), with poor results regarding the electrochemical properties (10^{-5} S cm^{-1}), despite presenting high densification values (83%).[37] Therefore, the formation of sodium phosphate phases under the harsh conditions in the present work was responsible for the worsening of the ionic conductivities in NaOH-processed samples. Although a minor phosphorus phase may be present when a basic TLP is employed, it is in such a low amount that it neither significantly alters the bulk crystal structure of NZZSP nor changes the overall sodium content, just
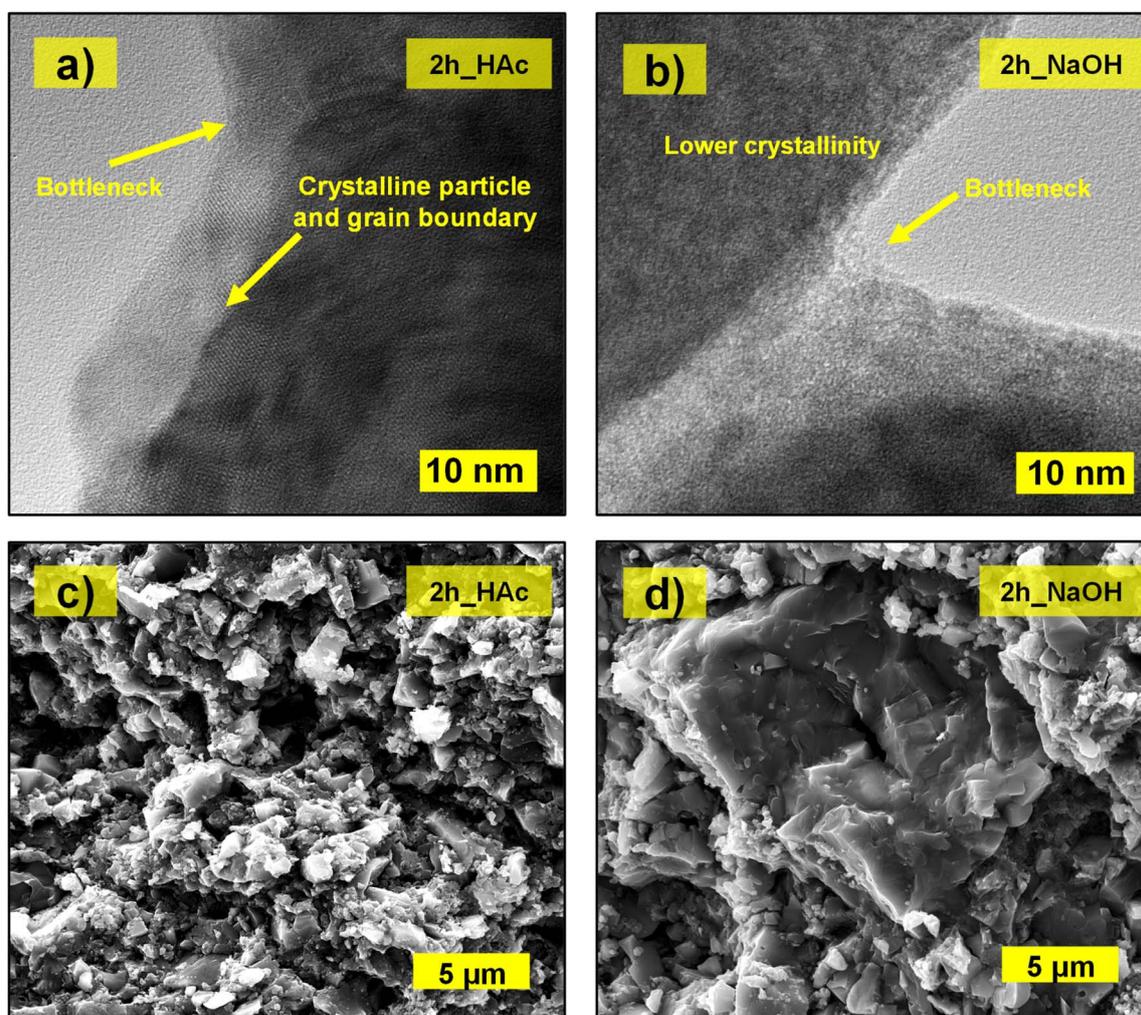

Fig. 5 (a and b) TEM images of NZZSP particles after cold sintering with acetic acid and sodium hydroxide, respectively. (c and d) Cross-section SEM images of NZZSP solid electrolytes after cold sintering with acetic acid and sodium hydroxide, respectively.

12444 | J. Mater. Chem. A, 2025, 13, 12439–12451

This journal is © The Royal Society of Chemistry 2025

influences the ionic conduction as this potentially new phase is formed at the grain boundaries of the ceramic particles, which limits the ionic conductivity. This phenomenon was also appreciable at a lower magnification through SEM images. As shown in Fig. 5(c) and (d), when HAc was employed, NZZSP particles remained angular and sharp, despite being modified due to the milling time. Yet, when NaOH was used as the TLP, particles appeared to be rounded and form smoother surfaces, as the one shown in the centre of the picture, due to the effect of the alkali. Images of SSEs cold sintered with the rest of milling times are shown in Fig. S6.† As a result, acetic acid was demonstrated to preserve intact the composition of the NZZSP electrolytes during the CSP as well as to produce SSEs with higher ionic conductivities (0.5–0.3 mS cm^{-1}), whereas the basic TLP (NaOH) appears to induce selective dissolution, particularly affecting phosphate species, which may lead to composition alterations and the formation of secondary phases in the grain boundaries, as suggested by the new small XRD peak and the morphological differences of the grain boundaries shown in the TEM micrographs. Consequently, for the study of doping with sodium ionic salts all the solid electrolytes were processed with HAc. Besides, only the NZZSP powders with 0 h and 2 h milling times were employed, since 4 h and 6 h were observed to produce similar values of ionic conductivity due to the resemblance in the particle size distribution.

Sodium ionic-salt doping

To study the effect of the ionic salts on NZZSP, NaTFSI and NaPF$_6$ salts were employed as Na$^+$ doping agents due to their relevance as ionic conductors in liquid electrolytes. Apart from the salts, different contents of them (0%, 10% and 20%) were also studied in order to evaluate the loading effect. Three replicas of every composition studied were produced, and the results shown here are the mean values of each series. Theoretically, the sodium salts incorporated through the HAc solution should precipitate in the grain boundaries of the particles
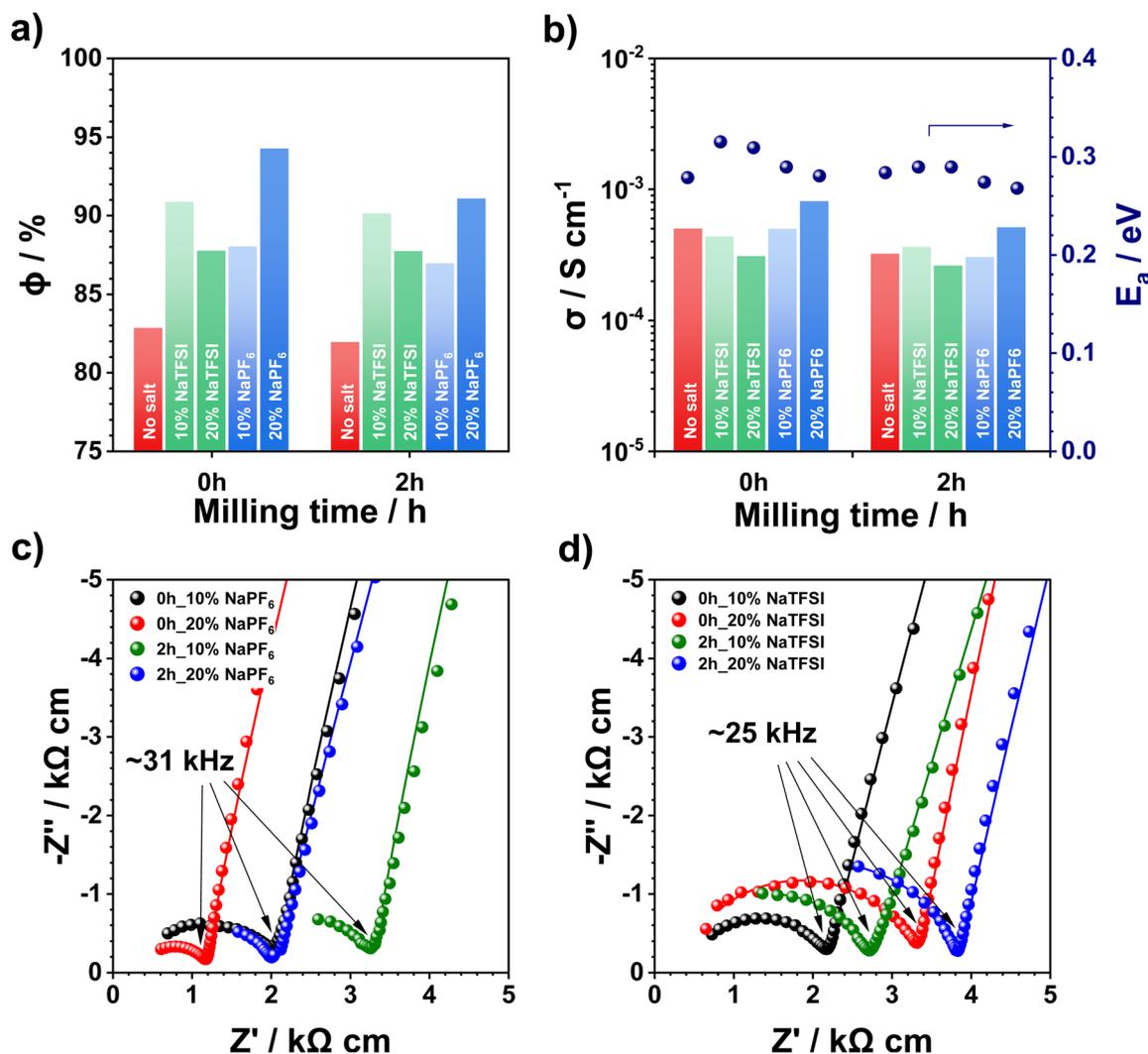

Fig. 6 Mean (a) relative density and (b) ionic conductivity and activation energies of NZZSP powders cold sintered with 0 h and 2 h powders and with different contents of NaTFSI and NaPF$_6$. (c and d) Nyquist plot and fitting of one series of solid-state electrolytes cold sintered with 0 h and 2 h powders and with different contents of NaTFSI and NaPF$_6$.

This journal is © The Royal Society of Chemistry 2025

J. Mater. Chem. A, 2025, **13**, 12439–12451 | **12445**

Table 2 Summary of the mean relative density, ionic conductivity, activation energy and particle size distribution as a function of the milling time and TLP employed in the CSP

t_{mill} (h)	0				2			
Salts	NaTFSI		NaPF$_6$		NaTFSI		NaPF$_6$	
Content (%)	10	20	10	20	10	20	10	20
φ (%)	90.9	87.7	88.0	94.3	90.1	87.7	86.9	91.1
σ (mS cm^{-1})	0.43	0.31	0.50	0.81	0.36	0.26	0.30	0.51
E_a (eV)	0.32	0.31	0.29	0.28	0.29	0.29	0.28	0.27

when the TLP is evaporated, with the morphology of the remaining salts being important to contribute as ionic diffusion channels of the sodium ions. As shown in Fig. 6(a), the addition of the ionic salts enhanced the microstructure of the resulting solid electrolytes in terms of densification, since they acted as pore-fillers when precipitated during the CSP. As a result, all the compositions produced presented a relative density value higher than that of the same solid electrolyte without the additive. Hence, it is confirmed that the ionic salts are deposited by filling the pores that were left in the microstructure of bare NZZSP. It was also noted that whilst a higher content of NaPF$_6$ in the electrolyte increased the relative density, in the

NaTFSI series the opposite occurred, as the 20% NaTFSI tested always produced lower values of relative density, indicating that an excess of NaTFSI could be worsening the densification. Thus, the solid electrolytes of 0 h and 2 h milling times with 20% NaPF$_6$ produced the highest densification values in their series, of 94.3% and 91.1% respectively.

Regarding the electrochemical properties, Fig. 6(b) describes the effect of the sodium ionic salt nature and content on the 0 h and 2 h series of NZZSP solid electrolytes. In general, the ionic conductivity of samples with ionic salt doping followed the same trend as densification, with an excess of NaTFSI harmful for ionic conductivity while a higher content of NaPF$_6$ appeared to be beneficial. Nonetheless, it was noted that in the case of the electrochemical properties, the addition of salts did not enhance the response as much as what was observed in densification. Here, there were only 3 cases that showed better results than the undoped solid electrolytes, which were 0 h_20% NaPF$_6$, 2 h_10% NaTFSI and 2 h_20% NaPF$_6$, with ionic conductivities of 0.81, 0.36 and 0.51 mS cm^{-1}, respectively. This enhancement of the ionic conductivity when these percentages of salts were added arises from the deposition of the salts on the surface of the NZZSP particles, providing a smoother grain boundary condition due to the higher conductivity of the salts with respect to the grain boundaries of the ceramics. As a result, a reduction of the overall grain boundary resistance is observed in the Nyquist plot of the doped composite electrolytes (Fig. 6(c)
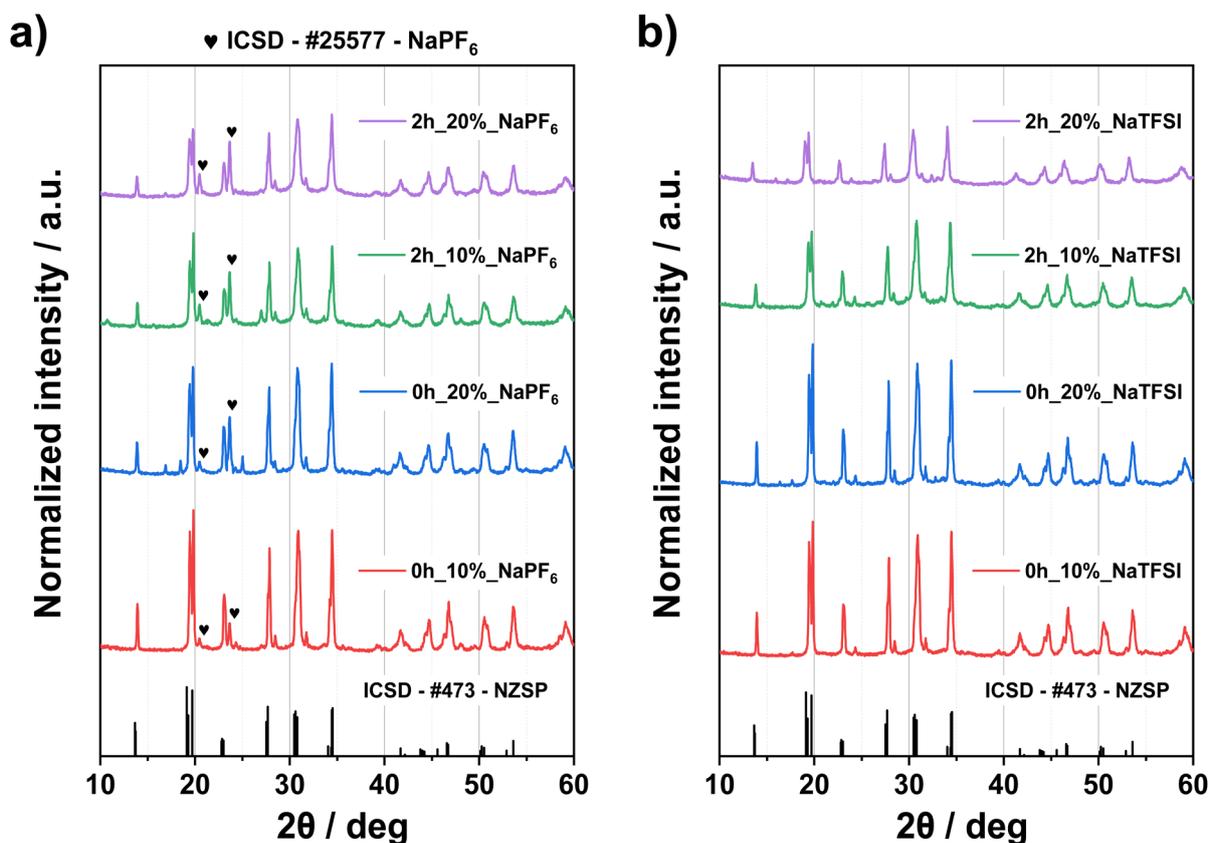

Fig. 7 (a) XRD patterns of NZZSP solid electrolytes cold sintered with 0 h and 2 h powders and with different contents of NaPF$_6$. (b) XRD patterns of NZZSP solid electrolytes cold sintered with 0 h and 2 h powders and with different contents of NaTFSI.

12446 | *J. Mater. Chem. A*, 2025, **13**, 12439–12451

This journal is © The Royal Society of Chemistry 2025

and (d)), supported by the increase in the frequency at which ionic transport is occurring (from 20 kHz to 31 kHz in the case of $NaPF_6$ and from 15 to 25 kHz in the case of NaTFSI). As for the activation energies, the general behaviour was that the samples with NaTFSI showed activation energies equal to or even higher than that of the undoped electrolytes, for both milling times series, whereas electrolytes with $NaPF_6$ showed activation energies close to that of the undoped electrolyte, or even lower in the case of 2 h_20% $NaPF_6$. Although activation energies did not show a great variation within the compositions tested, this indicated that the doping with ionic salts could not be beneficial in every case, as the ionic conductivity also suggested. All the electrochemical data are summarized in Table 2 and Arrhenius fittings for each series are shown in Fig. S7.†

In order to obtain a broader context of the effect of ionic salt doping on NZZSP, the microstructure was studied through XRD and SEM to check how the salts were affecting the electrochemical properties. Fig. 7 shows the obtained XRD patterns for the 0 h and 2 h series with $NaPF_6$ and NaTFSI, respectively. In the NaTFSI electrolytes, no variation was observed with the addition of the salt, probably due to the amorphous nature of the organic ionic salt, while in the $NaPF_6$ case two new peaks appeared at 20.2° and 23.4°, which coincided with the main peaks of $NaPF_6$ (ICSD #25577).[38] It was notably observed that a higher amount of added salt produced an increase in the relative intensity of its corresponding peaks, suggesting that there was more $NaPF_6$ being precipitated in the microstructure. This result was in line with the behavior of the relative density and ionic conductivity for the case of the $NaPF_6$ SSEs: an increase in the content of the salt resulted in an increase in the relative density and the ionic conductivities, reinforcing the idea that $NaPF_6$ deposited in the grain boundaries of the NZZSP particles was acting as a conductive channel as well as a pore filler. It was also remarkable that XRD patterns confirmed that the addition of the salts did not affect the crystalline structure of the NZZSP ceramics.

In this context, SEM images were obtained on the cross-section of the SSEs to investigate the morphology after doping
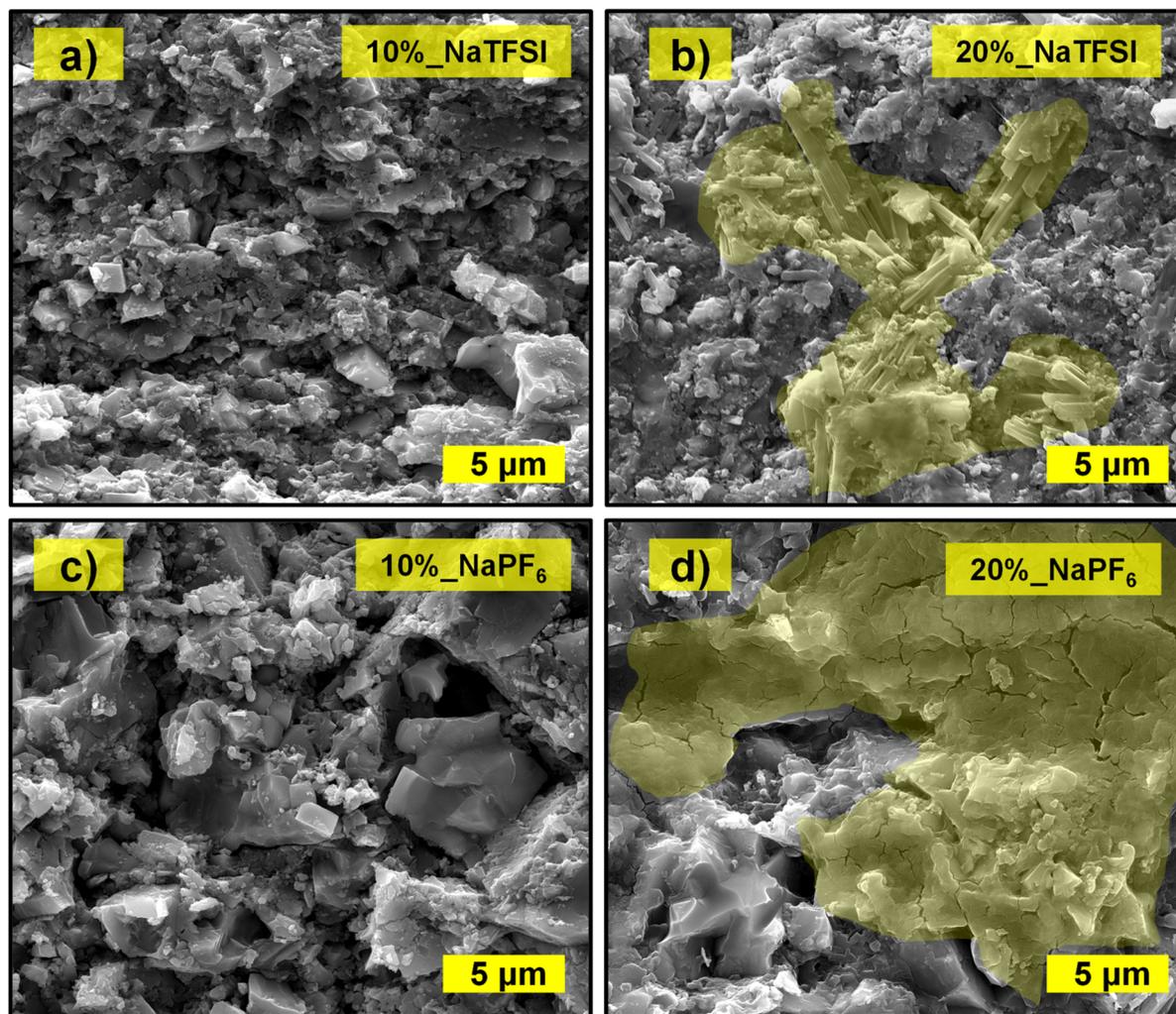

Fig. 8 (a and b) Cross section SEM images of the morphology of SSEs cold sintered with 2 h powder and with 10% and 20% of NaTFSI. (c and d) Cross section SEM images of the morphology of SSEs cold sintered with 2 h powder and with 10% and 20% of $NaPF_6$. SEM images of pure ionic salts are shown in Fig. S8 of the ESI.†

with the ionic salts. Fig. 8 depicts the microstructure of the 2 h solid electrolytes after the CSP with the doping agents. Although changes in the morphology of samples with only 10% of added salts were not appreciable, probably due to the low content of added salt, samples with 20% of the additive showed considerable differences. In the case of 20% NaTFSI (Fig. 8(b)), the salt appeared deposited in fibrous structures. Although NaTFSI is an organic molecule and could be malleable, the needle-like shape left in the structure could be responsible for the worsening of the ionic conductivity of these SSEs, as the shape did not contribute to the ionic pathways for Na^+ transport, producing less mobility or even an insulating network in the microstructure. In contrast, 20% $NaPF_6$ (Fig. 8(d)) in the SSEs appeared as a uniform matrix covering the surface of the internal microstructure once precipitated over the NZZSP particles. Fig. S8† shows SEM images of the pure salts deposited on a glass fibre membrane from the acetic acid solutions employed for the CSP of the doped solid electrolytes. Note that the cracks that appeared were not relevant, as they occurred due to high vacuum of the SEM. The morphology of this salt deposition resembled that of a PEO–LiTFSI matrix (poly(ethylene oxide)–lithium bis(trifluoromethanesulfonyl)imide) employed in previous reports.[28,39] In those cases, the polymeric matrix deposited on the microstructure functioned as a pore-filler while providing a smooth surface through which the Li^+ ions could be diffused in the case of lithium-based solid-state electrolytes, which resulted in an enhancement of the ionic conductivity.[40,41] Therefore, the similarity in the morphology of $NaPF_6$ deposited on the surface of those NZZSP solid electrolytes suggested that the ionic pathway produced by the salt, in parallel with the Na^+ transport of ceramics, was responsible for the enhancement of the ionic conductivity. As a result, NZZSP solid electrolytes produced with 0 and 2 hour milling times, with 20% of $NaPF_6$ (0 h_20% $NaPF_6$ and 2 h_20% $NaPF_6$) were eventually chosen to study the cycling behaviour, as that amount of salt was the only value that significantly improved the relative density and the ionic conductivity of the solid-state electrolytes.

Cycling performance

The first characterization study conducted on the NaSICON solid electrolytes doped with the ionic salt was a galvanostatic stability test performed in a symmetric cell configuration, using sodium metal as the electrode (Na|NZZSP–$NaPF_6$|Na) and 5 μL of liquid electrolyte to improve the interfacial contact between components of the cell, as neither interfacial modifications nor artificial solid electrolyte interfaces were used in order to study the present SSEs. Fig. 9(a) displays the cycling performance of 0 h_20% $NaPF_6$ and 2 h_20% $NaPF_6$ electrolytes in the symmetric cells, at a current density of 0.1 mA cm^{-2}. This current density is selected based on the results of the CCD characterization (shown in Fig. S9†), from which it is obtained that 0 h_20% $NaPF_6$ electrolytes can perform well without much overpotential until approximately 0.2 mA cm^{-2}, and the 2 h_20% $NaPF_6$ electrolytes until a current density of 0.3 mA cm^{-2}. In general, small fluctuations can be observed during the

cycling at constant current density, as the tests were performed under room conditions at a temperature of 20 ± 2 °C, with the variability associated with the environment. Even though the overpotential measured in the initial cycles was lower in the 0 h than in the 2 h series (0.05 V against 0.1 V vs. Na/Na^+), it rapidly increased during the initial 100 hours, reaching values of 0.15 V in contrast to the almost constant 0.1 V of the 2 h series. Finally, the 0 h_20% $NaPF_6$ electrolyte reached an overpotential higher than 1 V at approximately 200 hours of the test, which led to the shutoff of the cell due to safety concerns, whereas 2 h_20% $NaPF_6$ kept cycling for more than 500 hours, with a final measured overpotential of 0.15 V. The main reason behind this phenomenon could be attributed to dendrite growth through the pores and grain boundaries of the ceramics. Although the deposited salts play a key role as pore-fillers, ceramics processed by the CSP tend to leave microstructures with considerable amounts of bare grain boundaries. When the distribution of particle sizes is likely to produce great pore sizes, generally due to larger and coarser particles, the penetration and accumulation of electrode materials such as Li^0 and Na^0 during the plating and stripping process is favoured.[35,42,43] As a result, the gradual penetration of sodium metal led to the short circuit of the 0 h_20% $NaPF_6$ SSEs, similar to the case reported by Benben, W. et al. with a bare NZSP ceramic electrolyte with large grain sizes produced by solid-state sintering.[44] Indeed, detailed optical images of the surface of samples from 0 h_20% $NaPF_6$ after cycling (Fig. S10†) showed imprints near small cracks, comparable to those reported by the mentioned authors in their electrolytes, whereas 2 h_20% $NaPF_6$ did not show any remarkable degradation on the surface.

Additionally, SSEs of the same series were tested in half-cells containing $Na_3V_2(PO_4)_3$ as the cathodic active material (Na|NZZSP–$NaPF_6$|NVP) at multiple scan rates (with a theoretical discharge capacity C of 117.6 mA g_{NVP}^{-1} in 1 hour). Fig. 9(b)–(d) display the cycling performance of the 0 h- and 2 h-series of electrolytes evaluated at C/10, C/5, C/2 and 1C, during 5 cycles at each cycling rate. In line with previous results of the symmetric tests, the half-cells with 2 h_20% $NaPF_6$ achieved better results in all cases than those of 0 h_20% $NaPF_6$. Specifically, the 2 h-series reached specific discharge capacities of about 85 mA h g_{NVP}^{-1} at C/2, and remarkable values of over 100 mA h g_{NVP}^{-1} at C/10 after cycling at multiple higher rates, recovering almost all the initial capacity. Considering the differences in specific capacity of both types of half-cells, the effect of the dendrite growth fit as the main reason. In line with the symmetric cell results, as the cycling rate increased and time elapsed, the difference in specific capacity between the 0 h- and 2 h-series became larger, reinforcing the idea of a good microstructure preserving the electrochemical properties in the 2 h_20% $NaPF_6$–NZZSP solid state electrolytes. Overall, both types of NaSICON solid state electrolytes doped with ionic salts and produced by a low energy-demanding route, the cold sintering process, demonstrated superior electrochemical performance and a promising pathway to develop all solid-state sodium batteries coupled with proper development of stable interfaces and cathode materials.
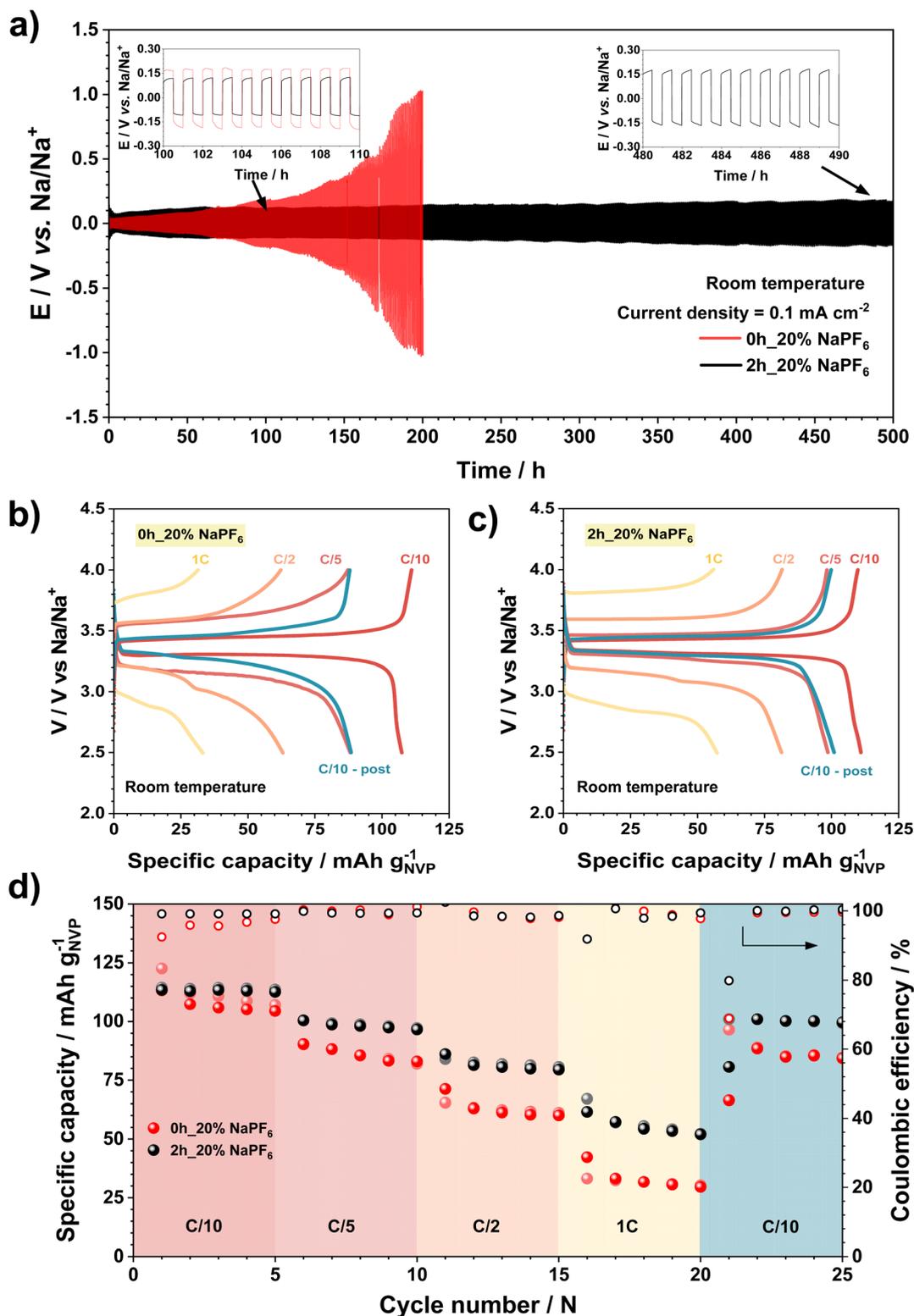
12448 | J. Mater. Chem. A, 2025, **13**, 12439–12451

This journal is © The Royal Society of Chemistry 2025

Fig. 9 (a) Cycling performance in Na symmetric cells of SSEs cold sintered with 20% NaPF$_6$ and 0 h (red) and 2 h (black) NZZSP powders. Current density is 0.1 mA cm^{-2}. (b and c) Specific charge and discharge capacities of NVP half-cells at different cycling rates for SSEs cold sintered with 20% NaPF$_6$ and 0 h (red) and 2 h (black) NZZSP powders, respectively. (d) Cycling performance of the half-cells at multiple cycling rates. All experiments are performed under lab conditions.

This journal is © The Royal Society of Chemistry 2025

J. Mater. Chem. A, 2025, 13, 12439–12451 | 12449

Conclusions

In this study, we reported the densification of $Na_{3.4}Zr_{1.9}Zn_{0.1}Si_{2.2}P_{0.8}O_{12}$ solid state electrolytes through the novel technique of the cold sintering process, which enabled the production of sustainable ceramic electrolytes at a low temperature of 150 °C with the aid of high pressure (720 MPa) and a transient liquid phase. Precisely, we studied the effect of the NZZSP milling time of the powder prior to the CSP, and how the particle size and distribution obtained affected the densification of the samples and their later microstructure. Furthermore, two different transient liquid phases (3 M HAc and 25 mM NaOH) were tested to evaluate the impact of the media on the densification mechanism and the resulting electrochemical properties. It was found that the alkaline media induced by NaOH produced morphological changes identified through a lower crystallinity of the NZZSP particles during the CSP, which resulted in worsening of the Na^+ transport properties ($\sigma = 0.25$ mS cm^{-1}), despite enabling a good densification degree ($\varphi > 82\%$). In contrast, the acetic acid medium retained a similar densification degree while also achieving an ionic conductivity two times higher ($\sigma = 0.50$ mS cm^{-1}, in the 0 h milling time powders). When composites were prepared by incorporating NaTFSI and $NaPF_6$ as sodium dopants in the CSP, with 10 wt% and 20 wt% of each salt added to the composition through the TLP, the morphological and electrochemical properties were evaluated. Regarding the densification degree, 20% of $NaPF_6$ enabled the highest relative density in each series of powders ($\varphi = 94.3\%$ and $\varphi = 91.1\%$ in the 0 h- and 2 h-series, respectively), and was the only percentage of salt that induced a significant improvement of the ionic conductivity ($\sigma = 0.80$ mS cm^{-1} and $\sigma = 0.51$ mS cm^{-1} in the 0 h_20% and 2 h_20% $NaPF_6$ series, respectively). Although 0 h_20% $NaPF_6$ SSEs produced the best results in terms of densification and ionic conductivity, when evaluated under operative conditions, the 2 h_20% $NaPF_6$ electrolytes demonstrated a better cycling behaviour. In symmetric cells (Na|NZZSP|Na) the 2 h-electrolytes remained stable with an overpotential of only 0.15 V for more than 500 hours, whereas the 0 h-samples had a short circuit at around 200 hours due to dendritic growth through a less stable microstructure. In line with these results, when tested in half cells (Na|NZZSP|NVP) at multiple scan rates, the 2 h_20% $NaPF_6$ SSEs always exhibited a higher and constant specific capacity value, achieving specific discharge capacities of about 85 mA h g_{NVP}^{-1} at C/2, and recovering almost all the initial discharge capacity, over 100 mA h g_{NVP}^{-1} at C/10 after cycling at multiple higher rates. Hence, this work demonstrates the potential of the cold sintering process for sustainable fabrication of high-performance sodium solid-state electrolytes, with the optimized composition being the 2 hour-milling time NZZSP with 20 wt% of $NaPF_6$ in a 3 M acetic acid solution achieving remarkable ionic conductivity and cycling stability, paving the way for potential solid-state sodium-ion batteries.

Data availability

The data supporting the results of this study are currently available from the corresponding author, N. V.-A., upon reasonable request, and the authors are awaiting approval to publish the data in the Universitat Jaume I repository.

Author contributions

Sergio Ferrer-Nicomedes: investigation, validation, and writing – original draft. Andrés Mormeneo-Segarra: investigation, validation. Nuria Vicente-Agut: supervision, review & editing. Antonio Barba-Juan: supervision, review & editing.

Conflicts of interest

There are no conflicts of interest.

References

1 P. V. Chombo and Y. Laoonual, *J. Power Sources*, 2020, **478**, 228649.

2 S. Chen, Z. Gao and T. Sun, *Energy Sci. Eng.*, 2021, **9**, 1647–1672.

3 H. Kim, H. Kim, Z. Ding, M. H. Lee, K. Lim, G. Yoon and K. Kang, *Adv. Energy Mater.*, 2016, **6**, 1600943.

4 P. K. Nayak, L. Yang, W. Brehm and P. Adelhelm, *Angew. Chem., Int. Ed.*, 2018, **57**, 102–120.

5 S. Chou, Y. Yu, S. Chou and Y. Yu, *Adv. Energy Mater.*, 2017, **7**, 1703223.

6 K. Takada, *J. Power Sources*, 2018, **394**, 74–85.

7 J. Janek and W. G. Zeier, *Nat. Energy*, 2023, **8**, 230–240.

8 J. Y. Hwang, S. T. Myung and Y. K. Sun, *Chem. Soc. Rev.*, 2017, **46**, 3529–3614.

9 J.-F. Wu, R. Zhang, Q.-F. Fu, J.-S. Zhang, X.-Y. Zhou, P. Gao, C.-H. Xu, J. Liu, X. Guo, J. Wu, R. Zhang, Q. Fu, J. Zhang, P. Gao, J. Liu, X. Zhou, X. Guo and C. Xu, *Adv. Funct. Mater.*, 2021, **31**, 2008165.

10 Z. Li, P. Liu, K. Zhu, Z. Zhang, Y. Si, Y. Wang and L. Jiao, *Energy Fuels*, 2021, **35**, 9063–9079.

11 C. Li, R. Li, K. Liu, R. Si, Z. Zhang, Y.-S. Hu and C. Zhizhen Zhang, *Interdiscip. Mater.*, 2022, **1**, 396–416.

12 Z. Moradi, A. Lanjan, R. Tyagi and S. Srinivasan, *J. Energy Storage*, 2023, **73**, 109048.

13 M. Guin, F. Tietz and O. Guillon, *Solid State Ionics*, 2016, **293**, 18–26.

14 H. Tian, S. Liu, L. Deng, L. Wang and L. Dai, *Energy Storage Mater.*, 2021, **39**, 232–238.

12450 | *J. Mater. Chem. A*, 2025, **13**, 12439–12451

This journal is © The Royal Society of Chemistry 2025

15 B. Xun, J. Wang, Y. Sato, G. Hasegawa, H. Akamatsu and K. Hayashi, *J. Mater. Chem. A*, 2025, **13**, 1766–1771.

16 H. Tian, S. Liu, L. Deng, L. Wang and L. Dai, *Energy Storage Mater.*, 2021, **39**, 232–238.

17 J. Guo, H. Guo, A. L. Baker, M. T. Lanagan, E. R. Kupp, G. L. Messing and C. A. Randall, *Angew. Chem., Int. Ed.*, 2016, **55**, 11457–11461.

18 A. Ndayishimiye, S. H. Bang, C. J. Spiers and C. A. Randall, *J. Eur. Ceram. Soc.*, 2023, **43**, 1–13.

19 N. Hamao, Y. Yamaguchi and K. Hamamoto, *Materials*, 2021, **14**, 4737.

20 Y. Zhang, A. Liu, Z. Shi, S. Ge and J. Zhang, *Int. J. Appl. Ceram. Technol.*, 2022, **19**, 320–331.

21 J. G. Pereira da Silva, M. Bram, A. M. Laptev, J. Gonzalez-Julian, Q. Ma, F. Tietz and O. Guillon, *J. Eur. Ceram. Soc.*, 2019, **39**, 2697–2702.

22 Y. Liu, Q. Sun, D. Wang, K. Adair, J. Liang and X. Sun, *J. Power Sources*, 2018, **393**, 193–203.

23 J. Yang, G. Liu, M. Avdeev, H. Wan, F. Han, L. Shen, Z. Zou, S. Shi, Y.-S. Hu, C. Wang and X. Yao, *ACS Energy Lett.*, 2020, **5**, 2835–2841.

24 C. Sun, B. Wang, L. Xie, H. Wang, Z. Li, Q. Zhang, L. Han and S. Dmytro, *Ceram. Int.*, 2024, **50**, 32930–32937.

25 Y. Li, Q. Wang, X. Zhao, B. He, Y. Xiao, J. Guo, L. Yang and R. Liao, *Ceram. Int.*, 2025, **51**, 1318–1325.

26 X. Zhu, K. Wang, Y. Xu, G. Zhang, S. Li, C. Li, X. Zhang, X. Sun, X. Ge and Y. Ma, *Energy Storage Mater.*, 2021, **36**, 291–308.

27 W. Liu, Q. Wang, Q. Ouyang, X. Zhang, Y. Wang, H. Tang, T. He, C. Yu, G. Li and L. Li, *J. Alloys Compd.*, 2024, **985**, 174065.

28 S. Ferrer-Nicomedes, A. Mormeneo-Segarra, N. Vicente-Agut and A. Barba-Juan, *J. Power Sources*, 2023, **581**, 233494.

29 A. Mormeneo-Segarra, S. Ferrer-Nicomedes, S. Simon, N. Vicente-Agut, J. C. Jarque-Fonfría and A. Barba-Juan, *Solid State Ionics*, 2024, **406**, 116482.

30 A. Mormeneo-Segarra, S. Ferrer-Nicomedes, N. Vicente-Agut and A. Barba-Juan, *J. Eur. Ceram. Soc.*, 2024, **44**, 5105–5114.

31 A. Mormeneo-Segarra, S. Ferrer-Nicomedes, N. Vicente-Agut and A. Barba-Juan, *Ceram. Int.*, 2023, **49**, 36497–36506.

32 Y. Li, Z. Sun, C. Sun, H. Jin and Y. Zhao, *Ceram. Int.*, 2023, **49**, 3094–3098.

33 A. J. Adetona, G. Wang, B. Walkley, D. C. Sinclair and I. M. Reaney, *J. Eur. Ceram. Soc.*, 2024, **44**, 2989–2997.

34 H. Y. P. Hong, *Mater. Res. Bull.*, 1976, **11**, 173–182.

35 S. Ferrer-Nicomedes, A. Mormeneo-Segarra, N. Vicente-Agut and A. Barba-Juan, *Ceram. Int.*, 2024, **50**, 44330–44338.

36 T. Sada, Z. Fan, A. Ndayishimiye, K. Tsuji, S. H. Bang, Y. Fujioka and C. A. Randall, *J. Am. Ceram. Soc.*, 2021, **104**, 96–104.

37 J. G. Pereira da Silva, M. Bram, A. M. Laptev, J. Gonzalez-Julian, Q. Ma, F. Tietz and O. Guillon, *J. Eur. Ceram. Soc.*, 2019, **39**, 2697–2702.

38 H. Bode and G. Teufer, *Z. Anorg. Allg. Chem.*, 1952, **268**, 20–24.

39 B. He, S. Kang, X. Zhao, J. Zhang, X. Wang, Y. Yang, L. Yang and R. Liao, *Molecules*, 2022, **27**, 6756.

40 W. Wang, E. Yi, A. J. Fici, R. M. Laine and J. Kieffer, *J. Phys. Chem. C*, 2017, **121**, 2563–2573.

41 J. Fu, Z. Li, X. Zhou and X. Guo, *Mater. Adv.*, 2022, **3**, 3809–3819.

42 S. Luo, Z. Wang, X. Li, X. Liu, H. Wang, W. Ma, L. Zhang, L. Zhu and X. Zhang, *Nat. Commun.*, 2021, **12**, 1–10.

43 L. Luo, Z. Sun, Y. You, X. Han, C. Lan, S. Pei, P. Su, Z. Zhang, Y. Li, S. Xu, S. Guo, D. Lin, G. Lin, C. Li, W. Huang, S. Wu, M.-S. Wang and S. Chen, *ACS Nano*, 2024, **18**, 2917–2927.

44 B. Wei, S. Huang, X. Wang, M. Liu, C. Huang, R. Liu and H. Jin, *Energy Environ. Sci.*, 2025, **18**, 831.

This journal is © The Royal Society of Chemistry 2025

J. Mater. Chem. A, 2025, **13**, 12439–12451 | **12451**